Lopsided gas discs arising from mass inflow in barred spiral galaxies

John L. Dupuy [ORCID],⋆ Fabian Heitsch⋆ and Gerald Cecil

Department of Physics and Astronomy, University of North Carolina at Chapel Hill, Chapel Hill, North Carolina 27514, USA

ABSTRACT

We explore numerically the effects of mass inflow on barred spiral galaxies in the context of high-velocity clouds accreting on to galactic discs. To assess whether such events are detectable, we quantify their effect on the disc's gas distribution by calculating the lopsidedness parameter A_1, and by deriving position–velocity plots of HI emission. The impact of an accretion event strongly depends on the parameters of the high-velocity cloud. For cloud mass $\geq 10^7$ $M_\odot$, infall can have a lasting impact on the gaseous disc, with $A_1 \gtrsim 0.05$ for ∼1.5 Gyr. We discuss the time-variability of the lopsidedness parameter and consequences for detecting gas infall. Accretion events will be marginally noticeable in position–velocity diagrams, again depending on cloud parameters. Our models provide a possible explanation for low-amplitude lopsidedness observed in galaxies without nearby companions.

Key words: methods: numerical – hydrodynamics – galaxies: spiral – galaxies: evolution.

1 INTRODUCTION

Lopsidedness of spiral galaxies describes the asymmetry in their visual light distribution, characterized by isophotes (Jog & Combes 2009). It was first noticed by Baldwin, Lynden-Bell & Sancisi (1980), who reported an asymmetry in the spatial extent of atomic hydrogen in the outer regions of four galaxies within their survey sample. Rix & Zaritsky (1995) explored lopsidedness systematically and developed the current standard definition of lopsidedness as the fractional amplitude of the first azimuthal Fourier component ($m = 1$) of the surface brightness (A_1). Approximately, 1/3rd of their sample of 18 galaxies display significant lopsidedness ($A_1 >$ 0.2) at 2.5 disc exponential scale lengths (Rix & Zaritsky 1995). These results were later corroborated by Zaritsky & Rix (1997) in their survey of 60 spiral galaxies ∼30 per cent of which displayed significant lopsidedness. In their observational and theoretical study, Bournaud, Jog & Combes (2005) reported ∼30 per cent of their 149 observed galaxies to be lopsided. With the help of *N*-body simulations, they found that strong lopsidedness can result from minor mergers, tidal encounters, and cosmic gas accretion on time-scales of 1–3 Gyr. Of the three, only cosmic gas accretion can explain the large frequency of strong lopsidedness in galaxies that are isolated with no companion and no sign of a recent merger (Bournaud et al. 2005; Jog & Combes 2009). Reichard et al. (2008) studied lopsidedness in ∼25 000 low-redshift ($z < 0.06$) galaxies from the Sloan Digital Sky Survey (SDSS). They found that the majority of the galaxies in their sample display some lopsidedness.

We explore how gas infall can cause lopsidedness in the gas distribution of barred spiral galaxies. About 70 per cent of spiral galaxies contain a bar, i.e. their stellar distribution is elongated rather than azimuthally symmetric (Eskridge et al. 2000). The role of stellar bars in galaxies is extremely well established (Contopoulos & Papayannopoulos 1980; Binney et al. 1991). The elongated gravitational potential due to a stellar bar exerts gravitational torques on the gas. The resulting orbits self-intersect, which leads to gas collision, compression, and angular momentum loss as the gas shifts from orbits along the major axis of the bar (x_1 family) to orbits along the minor axis of the bar (x_2 family). Numerical studies have shown that the funneling of gas to the galactic centre can enhance star formation (Athanassoula 1992b; Kim et al. 2011, 2012).

The interplay of the bar with the $m = 1$ lopsided mode could possibly explain why lopsidedness is so prevalent.[1] Here, we introduce lopsidedness via gas accretion on to the disc of a barred spiral galaxy. We explore a parameter space that aims to represent the infall of high-velocity clouds (HVCs). HVCs are identified as gas clouds with radial velocities $|v_{LSR}| > 100$ km s^{-1}, that is, clouds that do not fit a standard Galactic rotation pattern (Putman, Peek & Joung 2012). The Milky Way's HVC population is estimated to have a neutral gas mass of ∼ 10^8 $M_\odot$, with an accretion rate on to the Galactic disc of ∼0.5 $M_\odot$ yr^{-1} (Wakker & van Woerden 1997; Wakker et al. 2007, 2008; Putman et al. 2012). A prime example for the scenario envisioned in this study is the trajectory of the Smith cloud (Lockman et al. 2008; Nichols & Bland-Hawthorn 2009). The Smith Cloud is a massive system of metal-poor neutral and ionized gas with a lower mass limit of $M_{gas} > 2 \times 10^6$ $M_\odot$ (Fox et al. 2016). M31 and other nearby galaxies show neutral hydrogen structures in their haloes, suggesting that HVCs are a common galactic phenomenon (Thilker et al. 2004; Sancisi et al. 2008).

---

[1]Another infall signature in three dimensions would be an extra-planar component of the perturbed gas disc compared to the settled stellar disc.

⋆ E-mail: jdupuy26@live.unc.edu (JLD); fheitsch@email.unc.edu (FH)

We perform 2D grid-based simulations of gas accretion on to the disc of a barred spiral galaxy, discussing the following questions: (1) for how long does the signature of infall survive in a galactic disc; (2) how does the perturbed disc evolve in the elongated bar potential; (3) how do the signatures of infall depend on the infall parameters; and finally, (4) how well can gas infall explain lopsidedness in spiral galaxies.

Simulation methods and analysis tools are introduced in Section 2. Section 3 presents our fiducial inflow event and corresponding position–velocity diagrams for 'observational' comparison. A discussion and a summary can be found in Section 4.

2 METHODS

2.1 Hydrodynamics

We use a modified version of the Eulerian grid code Athena 4.2 (Stone et al. 2008) to solve the equations for inviscid, compressible hydrodynamics in 2D,

$$\frac{\partial \Sigma}{\partial t} + \nabla \cdot (\Sigma \mathbf{v}) = S_{c,\Sigma}, \tag{1}$$

$$\frac{\partial \Sigma \mathbf{v}}{\partial t} + \nabla \cdot (\Sigma \mathbf{v} \mathbf{v} - P\mathbb{1}) = \mathbf{S}_{c,M} + \mathbf{S}_{g,M}, \tag{2}$$

$$\frac{\partial E}{\partial t} + \nabla \cdot [(E + P)\mathbf{v}] = S_{c,E} + S_{g,E} + S_{\mathcal{L},E}. \tag{3}$$

The mass surface density is given by Σ, where $\mathbf{v}$ is the velocity, $E = \Sigma \mathbf{v}^2/2 + P/(\gamma - 1)$ is the total energy density, $\mathbb{1}$ is the unit dyadic, and P is the (surface) pressure. The mass, momentum, and energy source terms for the cloud inflow ($S_{c,\Sigma}$, $\mathbf{S}_{c,M}$, $S_{c,E}$), the gravitational potential ($\mathbf{S}_{g,M}$, $\mathbf{S}_{g,E}$), and heating and cooling ($S_{\mathcal{L},E}$) are discussed below. We set $\gamma = 5/3$.

To solve equations (1)–(3), we use the HLLC solver in combination with a 3rd-order Runge–Kutta method (Toro, Spruce & Speares 1994; Gottlieb & Shu 1998). We integrate the equations on a 2D, cylindrical mesh with coordinates (R, ϕ) (see Skinner & Ostriker 2010, for an implementation into Athena). To keep the aspect ratio of the cells constant, we use a logarithmic radial grid,

$$R_i = (1 + \delta) R_{i-1},$$
$$1 + \delta = \left(\frac{R_f}{R_0}\right)^{1/N_R}, \tag{4}$$

where R_0, R_f are the minimum and maximum radii for the grid, and N_R represents the number of cells in the R-direction. For our simulations, $R_0 = 10$ pc, $R_f = 15$ kpc, and $N_R = 512$. At R_0, this gives a peak resolution of $\delta R_0 \approx 0.144$ pc, while at R_f, the resolution degrades to $\delta R_f \approx 213$ pc. The grid in the ϕ direction is uniform and the number of cells in the ϕ-direction is the same as that in the R-direction, $N_\phi = N_R = 512$. The azimuthal coordinate ϕ ranges from 0 to 2π. Boundary conditions are set to outflow-only at the inner and outer R boundary, while the domain is periodic in ϕ.

We select initial conditions intended to replicate the Galaxy (Bensby, Feltzing & Lundström 2003; Binney & Tremaine 2008; Sormani et al. 2018). An initial gas surface density $\Sigma_0 = 10$ M$_\odot$ pc^{-2}, a constant scale-height of $h_s = 300$ pc appropriate for the thin disc, and a mean molecular weight of $\mu = 1$, results in an initial number density of

$$n_0 = \frac{\Sigma_0}{h_s \mu m_H} = 1.348 \text{cm}^{-3}, \tag{5}$$

where m_H is the hydrogen mass. The initial thermal pressure is set by the equilibrium temperature due to the balance between heating and cooling. For our choice of metallicity, scale height, and initial density, this turns out to be $P_{eq} \approx 8.22 \times 10^3$ K cm^{-3} for $R \lesssim 9$ kpc. Past 9 kpc, the metallicity gradient causes P_{eq} to increase to a maximum value of $P_{eq} \approx 1.02 \times 10^4$ K cm^{-3} for $R = 15$ kpc (cf. Section 2.3 for more detail).

We start gas on circular orbits determined by

$$v_c(R) = \sqrt{R \frac{d\Phi_0}{dR}}, \tag{6}$$

where Φ_0 is the initial (axisymmetric) gravitational potential. The non-axisymmetric part of the gravitational potential is introduced by ramping up its strength linearly with time between 5 Myr and 155 Myr. This allows time for the disc to reach a steady state as the gas settles into orbits around the bar.

2.2 Static gravitational potential

Following Kim et al. (2012) and Jung, Illenseer & Duschl (2018), the gravitational potential consists of three components: (i) disc, (ii) bulge, and (iii) bar. We exclude the black hole potential of Kim et al. (2012) as this work does not focus on accretion on the Galaxy's central black hole.

The stellar disc of the Galaxy is represented by a Kuzmin–Toomre model (see Binney & Tremaine 2008) of the form

$$\Phi_d(R) = -\frac{GM_{\text{disk}}}{\sqrt{R^2 + (R_0 + R_1)^2}}, \tag{7}$$

where $M_{\text{disc}} = 2.2 \times 10^{11}$ M$_\odot$, $R_0 = 14.1$ kpc, and $R_1 = 14.1$ pc.

The stellar bulge is represented by a modified spherically symmetric Hubble profile (Binney & Tremaine 2008),

$$\Phi_{\text{bul}}(R) = -\frac{4\pi G \rho_{\text{bul},0} R_b^3}{R} \log\left(\frac{R}{R_b} + \sqrt{1 + \frac{R^2}{R_b^2}}\right), \tag{8}$$

with $\rho_{\text{bul},0} = 24$ M$_\odot$ pc^{-3} and $R_b = 0.33$ kpc.

The bar is modelled using a Ferrers ellipsoid for the underlying stellar distribution (Pfenniger 1984, and references therein. See also Athanassoula 1992a,b; Romero-Gómez et al. 2007; Kim et al. 2012). The density distribution is given by

$$\rho(g) = \rho_{b,0} \begin{cases} (1 - g^2)^n & ; g < 1, \\ 0 & ; g \geq 1. \end{cases} \tag{9}$$

Here, $n = 1$, $\rho_{b,0} = 0.45$ M$_\odot$ pc^{-3}, and $g^2 = x^2/a^2 + y^2/b^2 + z^2/c^2$, with the principal semi-axes (a, b, c) in Cartesian coordinates (x, y, z). The stellar distribution of the bar does not extend beyond $g = 1$. We select $(a, b, c) = (5, 2, 1.8)$ kpc. With $n = 1$, the mid-plane $(z = 0)$ potential has the form

$$\Phi_b(x, y, 0) = -\frac{\pi G abc \rho_{b,0}}{2} \\ \times \left[W_{000} + x^2\left(x^2 W_{200} + 2y^2 W_{110} - 2W_{100}\right) \\ + y^2\left(y^2 W_{020} - 2W_{010}\right)\right], \tag{10}$$

where the W_{ijk} coefficients are defined in Pfenniger (1984). We selected these parameters to match Kim et al. (2012) and Jung et al. (2018). The quadrupole moment of the bar is equal to $Q_m = M_b(a^2 - b^2)/7 = 4.2 \times 10^{10}$ M$_\odot$ kpc^2. M_b is the mass of the bar and is equal to $M_b = (32/60)\pi abc \rho_{b,0} = 1.4 \times 10^{10}$ M$_\odot$. Fig. 1 summarizes the rotation curve for the various potential components, and the angular speed (see figs 1 and 2 of Kim et al. 2012 for comparison,
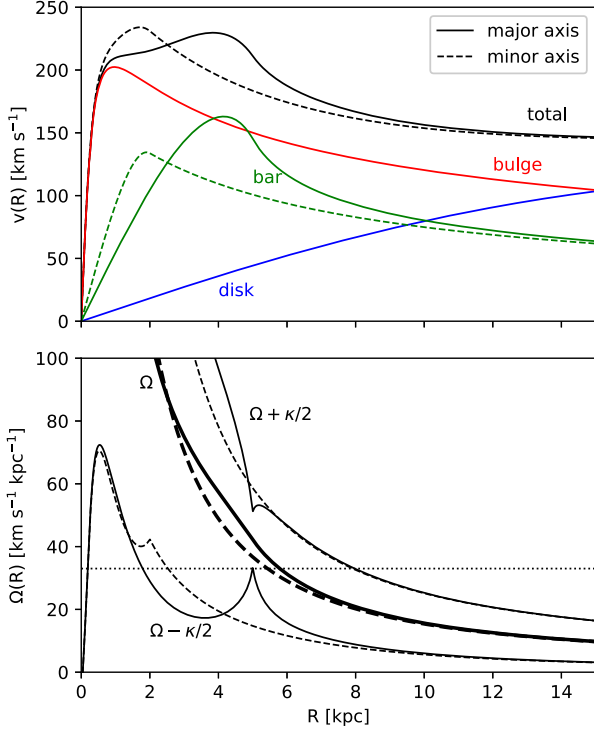
Figure 1. Rotation curves for galaxy components as indicated (top), and angular speeds (bottom), for comparison with figs 1 and 2 of Kim et al. (2012). The dotted line indicates the bar pattern speed of 33 km s^{-1} kpc^{-1}.

specifically their case without a central black hole). The potential shows the two inner Lindblad resonances discussed by Kim et al. (2012). A third Lindblad resonance seems to be suggested at 5 kpc, yet that far out, the potential is not axisymmetric.

2.2.1 Source terms

We solve the fluid equations in a coordinate system co-rotating with the bar, at a rate of $\Omega_b = 33$ km s^{-1}kpc^{-1}. Therefore, centrifugal and Coriolis forces need to be added to the source terms,

$$S_{g,M} = -\Sigma(\nabla\Phi_{\rm eff} - 2\Omega \times \mathbf{v}), \tag{11}$$

for the momentum equations, and

$$S_{g,E} = -\Sigma\mathbf{v} \cdot \nabla\Phi_{\rm eff}, \tag{12}$$

for the energy equation. Here, $\Phi_{\rm eff} = \Phi_b + \Phi_d + \Phi_{\rm bul} - 0.5\Omega_b^2 R^2$, $\Omega = (0, 0, \Omega_b)$. In equation (12), we have used the fact that $\mathbf{v} \cdot (\Omega \times \mathbf{v}) = 0$.

2.3 Heating and cooling

To model the thermal physics of the gas, we include the effects of heating and radiative cooling. The corresponding source term is given by,

$$S_{\mathcal{L},E} = n\Gamma - n^2\Lambda, \tag{13}$$

where n is the number density. The heating rate Γ is given in ergs s^{-1}, and $n^2\Lambda$ is the volumetric cooling rate with units ergs s^{-1}cm^{-3}. Λ includes temperature and metallicity ([Fe/H]) dependence. Heating and cooling are implemented as a look-up table generated by MAPPINGS V (Sutherland & Dopita (1993); Dopita et al. (2013, 2016)). Given inputs of n, T, and [Fe/H], cooling
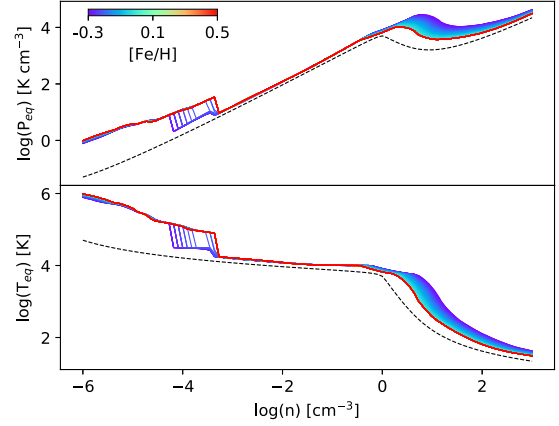

Figure 2. The equilibrium curves $P_{\rm eq}(n)$ and $T_{\rm eq}(n)$ as [Fe/H] are varied. Coloured lines show the variation of equilibrium temperature and pressure within the range of metallicities encountered in the model disc. The dashed black line represents the equilibrium curve of Koyama & Inutsuka (2002).

rates are linearly interpolated from this table to determine how the thermal energy changes during an integration step. The source term (equation (13)) is added in an operator-split fashion to the energy equation. To prevent over-cooling, the ordinary differential equation $\dot{e} = n\Gamma - n^2\Lambda$ is solved via an adaptive stepsize Runge–Kutta–Fehlberg method, integrating over a hydrodynamical CFL time-step of Δt. Then, $S_{\mathcal{L},E} = \dot{e}$. For the current application in combination with the third-order time update, this is sufficiently accurate.

For the metallicity dependence of radiative losses, we adopt a linear extrapolation of an estimate of the Galactic metallicity-gradient based on a linear fit to the metallicities of 265 Cepheid variable stars (Pedicelli et al. 2009). At the Galactic centre, we assume a metallicity of [Fe/H]=0.45. Past $R = 0$ kpc, the metallicity decreases with increasing galactocentric distance at a constant rate of -0.05 dex kpc^{-1}.

Fig. 2 plots the equilibrium curves for a variety of [Fe/H] values in the range of our metallicity gradient ($-0.3 <$ [Fe/H] <0.5). We see that our loss table provides more heating (and less cooling) overall than Koyama & Inutsuka (2002). This is particularly true at low n. Evident from these panels is the small influence of the metallicity gradient. Metallicity variations affect the cooling strength mostly for low temperatures, because the cooling is dominated by fine-structure lines of metals in this regime. For high temperatures, cooling is dominated by Lyman-α (at 10^4 K) and free–free emission.

2.4 Dual energy formulation

In some regions of our simulations, flow conditions can become extreme in the sense that the kinetic energy dominates the internal energy by several orders of magnitude. In such cases, the pressure calculated from the total energy density, $P = (\gamma - 1)(E - 0.5\Sigma\mathbf{v}^2)$ can become negative in the reconstruction step. This tends to occur in the ring of x_2 orbits, where density and velocity (in the rotating frame) are high. The high density of the gas results in a small thermal energy, while the high velocity results in a large kinetic energy. While a pressure floor would allow the simulation to continue, it would lead to unphysical cooling rates. Therefore, we use a modified version of the dual energy formalism described by Bryan et al. (2014) and Goodson et al. (2016). The formalism solves the equations for the total and internal energy equation at each time-step, reverting to the internal energy density if the pressure $P < 0$. If

Table 1. Parameter values for cloud inflow.

Parameter	Values	Units	Description
Δt_c	20	Myr	time of infall
M_c	5×10^6, **10^7**	$M_\odot$	cloud mass
r_c	0.5, **1.0**	kpc	cloud radius
$r_{\text{pos},0}$	5.5, 6.5, **7.5**, 10	kpc	cloud position
f_c	**-1.0**, 1.0, 2.0	N/A	cloud velocity

the total energy equation yields $E > 0$ after the time-step, the internal energy is re-initialized as $e = E - 0.5\Sigma v^2$ for the subsequent step.

2.5 Mass inflow

Starting with a steady state bar simulation, we assume that a cloud of mass M_c represented by a cylindrical column of radius r_c is accreted on to the Galactic disc over a time-scale Δt_c. Because our models are 2D, this accretion is implemented as mass, momentum, and energy source terms,

$$S_{c,\Sigma} = \frac{M_c/\Delta t_c}{\pi r_c^2}, \tag{14}$$

$$\boldsymbol{S}_{c,M} = S_{c,\Sigma}\boldsymbol{v}_c, \tag{15}$$

$$S_{c,E} = \frac{1}{2}S_{c,\Sigma}v_c^2. \tag{16}$$

In the rotating frame, the cloud's velocity vector is given in cylindrical coordinates by $\boldsymbol{v}_c = [0.0, -f_c\Omega_b r_{\text{pos},0}]$, where f_c sets the ϕ velocity of the cloud material. In an inertial frame, this corresponds to a velocity $v'_{c,\phi} = (1 - f_c)\Omega_b r_{\text{pos},0}$.

We have run 40 simulations with various combinations of the inflow parameters to explore the parameter space. The values for the inflow parameters are summarized in Table 1. Boldfaced numbers indicate parameters for the fiducial run.

2.6 Lopsidedness measure

We use the standard definition of the lopsidedness measure (Rix & Zaritsky 1995; Bournaud et al. 2005; Jog & Combes 2009) to quantify the influence of the mass accretion on the galactic disc. This measure is used observationally to determine the lopsidedness in the surface brightness distribution of stars in galaxy surveys. Here, we apply this measure to the surface density distribution of gas. The lopsidedness measure is found by decomposing the surface density (Σ) into its radial and azimuthal Fourier components,

$$\Sigma(R, \phi, t) = a_0(R, t) + \sum_{m=1}^{\infty} a_m(R, t)\cos(m\phi - \phi_m(R, t)), \tag{17}$$

where a_m is the amplitude of mode m and ϕ_m is the associated phase. The normalized strength of a Fourier component is then defined as

$$A_m(R, t) = \frac{a_m(R, t)}{a_0(R, t)}, \tag{18}$$

such that $A_1(R, t)$ represents the normalized amplitude of the disc lopsidedness at a given radius and time. We define $\langle A_1 \rangle(t)$ as the radial average of A_1 between 5 kpc and 12 kpc at a given time, excluding the bar region and focusing upon lopsidedness in the outer disc of the Galaxy. The radial range for averaging is consistent with observational analyses. Bournaud et al. (2005) restrict averages

between 1.5 and 2.5 exponential scale radii, and Reichard et al. (2008) limit the range between the Petrosian radii R_{50} and R_{90}.

2.7 Position–velocity diagrams

We generate synthetic position–velocity[2] diagrams of 21-cm HI emission from the viewpoint of several observers. The calculation of the (l, v) diagrams is implemented as an on-the-fly analysis in Athena. For a number of velocity channels, we integrate the equation of radiative transfer in the optically thin limit along rays emanating from an observer's position. We explore four observer positions, one within the galactic disc, and three intended to mimic observing the Andromeda galaxy. The positions of these observers with respect to the centre of our grid are

$$\mathbf{r}_{\text{obs},0} = [R_\odot, 160°],$$
$$\mathbf{r}_{\text{obs},1} = [R_{\text{and}}, 0°],$$
$$\mathbf{r}_{\text{obs},2} = [R_{\text{and}}, 45°],$$
$$\mathbf{r}_{\text{obs},3} = [R_{\text{and}}, 90°]. \tag{19}$$

In equation (19), $R_\odot = 8$ kpc, and $R_{\text{and}} = 778$ kpc, the distance from the Milky Way to Andromeda. For observers external to the disc, we assume that we are viewing the galaxy edge-on and trace rays in an angular extent such that they encompass the whole grid. If the observer is inside the disc, we calculate rays in every direction, to get a 360° perspective of the gas.

To generate a specific (l, v) map, we linearly interpolate density, radial momenta, and total energy on to a ray and compute the local number density n, velocity v, and temperature T from the interpolated quantities. From v, we compute the line of sight velocity (v_{los}) via

$$v_{\text{los}} = [\Omega(R) - \Omega(r_{\text{obs}})]r_{\text{obs}}\sin l, \tag{20}$$

(see Binney & Merrifield 1998, their Section 9.1). Here, $\Omega(R) = v/R$, with v as the velocity of gas in the (inertial) simulation frame, and $\Omega(r_{\text{obs}}) = v_{\text{obs}}/r_{\text{obs}}$. We assume all observers are on circular orbits with $v_{\text{obs}} = 220$ km s^{-1} and r_{obs} given by one of equation (19). For observers external to the disc, v_{obs} is negligible and $v_{\text{los}} \approx \Omega(R)r_{\text{obs}}\sin l$. If the observer is in the disc, l is the (Galactic) longitudinal angle. Otherwise, l is the angle between a line from the observer to the centre of the galaxy and the ray. Regardless, $\sin l$ is given by the geometric relation,

$$\sin l = \frac{R\sin\phi}{|\mathbf{R} - \mathbf{r}_{\text{obs}}|}, \tag{21}$$

where (R, ϕ) are the usual cylindrical coordinates, and $\mathbf{R}$ denotes the radius vector. The brightness temperature $T_B(v_{\text{ch}})$ is calculated for each velocity channel v_{ch} as the sum over all positions along the ray contributing to that channel. We assume thermal broadening of gas at each position, based on the local temperature. Thus, the brightness temperature is given by

$$T_B(v_{\text{ch}}) \approx 2.2 \times 10^{-29}$$
$$\times \int \frac{n(s)}{\sigma} \exp\left(-\frac{(v_{\text{ch}} - v_{\text{los}}(s))^2}{2\sigma^2}\right) ds \ \ [\text{K}], \tag{22}$$

where n is the number density, v_{los} is the line-of-sight velocity, and σ is the sound speed of the gas along the ray (s). The constant factor in equation (22) assumes CGS units for all quantities.

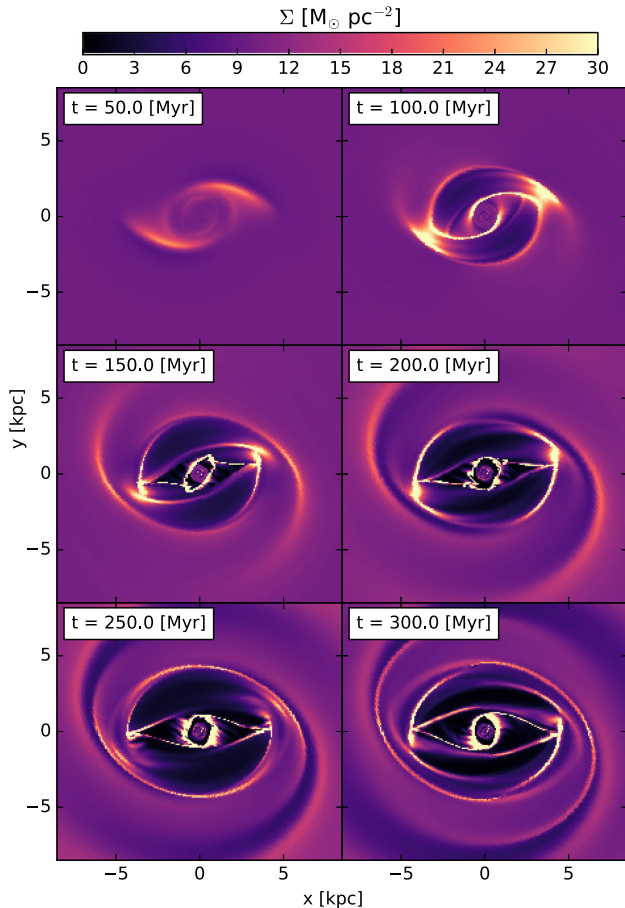[2]In the following, we refer to these as (l, v) diagrams.

Figure 3. Snapshots of surface density (Σ) during the build-up of the bar by slowly introducing the bar potential. At 300 Myr, a steady state has been reached, which forms the starting point of the subsequent infall models.

Our velocity channels have a resolution of 1.5 km s^{-1} and the boundaries are set by min/max(v_{los}). The number of rays for all observers is fixed at 700 and the number of points along the ray varies from around 10^2 to 10^3, depending on where the ray cuts through the grid.

3 RESULTS

3.1 Creating barred orbits

To generate a steady state model of gas flow in a barred spiral galaxy, we follow the approach of Jung et al. (2018) and Kim et al. (2012). We introduce the bar potential slowly in an initially azimuthally symmetric galaxy. From $t = 5$ Myr to $t = 155$ Myr, we ramp up the strength of the bar potential. To mitigate radial perturbations when introducing the bar, mass is removed from the bulge at the same rate as it is added via the bar (Kim et al. 2012). The transition is shown in Fig. 3.

When the bar potential is introduced, angular momentum is removed from the gas via gravitational torques, and the bar 'shocks' start to form (Fig. 3 at $t = 50$ Myr). As the strength of the bar potential increases, the shocks become more prominent. The characteristic orbits discussed in Athanassoula (1992b) begin to form. Due to the logarithmic grid, the high resolution at the centre of our mesh allows us to resolve x_2 orbits in and around the central 'nuclear' ring. This is evidenced by the central disc of high density

material that orbits near the inner R-boundary. High velocities and density gradients give rise to the 'wiggle instability' seen in the x_2 orbits of the $t = 150, 200,$ and 250 Myr snapshots (Wada & Koda 2004; Kim, Ostriker & Kim 2014). After the bar potential has reached full strength, two spiral arms start to form.

Orbits in barred potentials have been discussed at length (Athanassoula 1992a; Sormani, Binney & Magorrian 2015; Ridley et al. 2017; Sormani et al. 2018), so we will only briefly mention a few features here. Away from the bar ends at 5 kpc, the gas approximately follows closed orbits of the x_1 family. Due to angular momentum loss, the gas will drift towards the cusped x_1 orbit. At the cusp, orbits of the x_1 family become self-intersecting, and gas builds up at the bar ends. The density in these regions is around $2-3$ times the ambient density (cf. $t = 150$ Myr panel of Fig. 3). As the gas flows collide, shocks form, and the gas is funneled towards the Galactic centre (gas lanes seen in $t = 150-300$ Myr panels). When the gas reaches the centre, it settles into a ring of x_2 orbits.

Because the stellar and halo components of the Galaxy are fixed in our model, the spiral arms that develop are driven by the bar potential (cf. Sormani et al. 2015). The potential we have selected was studied in depth in the context of manifold-driven spiral arm and ring formation (Romero-Gomez et al. 2006, 2007). In a frame that rotates with the bar, our potential has five Lagrange points: three along the semi-minor axis of the bar (L_4, L_3, L_5), and two along the semi-major axis of the bar (L_1, L_2). The points $L_3, L_4,$ and L_5 are stable but L_1 and L_2 are not. Romero-Gomez et al. (2006) propose that rings and spiral arms comprise of stable and unstable invariant manifolds associated with the Lyapunov orbits around L_1 and L_2. These manifolds can be thought of as collections of periodic orbits that, when evolved in time, move towards (stable case) or away from (unstable case) the L_1 or L_2 equilibrium points. Romero-Gómez et al. (2007) evolved these orbits forward and backward in time using a potential model nearly identical to our own (cf. fig. 8 of Romero-Gómez et al. (2007), with $r_L = 6.5$). The result is a manifold of orbits that traces out spiral arms, and eventually a ring reminiscent of e.g. NGC 1326.

These manifolds initially form very slowly, then evolve more rapidly at late times (cf., fig. 6 of Romero-Gomez et al. (2006)). This behaviour is clearly seen in our model, as gas begins to align itself with these orbits around $t = 150-300$ Myr, and the spiral arms rapidly expand outwards from $t = 350-1000$ Myr. At $t = 800$ Myr, a distinct ring-structure in the gas is seen. How mass infall during the evolution of these manifolds will affect the disc's lopsidedness will be discussed in the next section.

3.2 A fiducial inflow event

*****Fig. 4 shows a time series of the surface density Σ for a representative inflow event with a cloud mass of 10^7 M$_\odot$ at $R_{gc} = 7.5$ kpc, orbiting initially with the bar ($f_c = -1.0$). Because this radius lies beyond the corotation radius, the gas flow in the rotating frame is counterclockwise, while the cloud (initially) orbits clockwise. The $t = 350$ Myr snapshot shows the influence of the cloud 25 Myr after all of its mass has been deposited on to the disc. Upon infall, collisions between the disc and cloud material slow the flow of the gas, resulting in large density variations in the gas. These density variations will contribute significantly to lopsidedness in the disc. Though the cloud is initially on a clockwise orbit in the rotating frame, it is quickly swept up by the gas on counter-clockwise orbits, and starts on an orbit in that direction.

As this occurs, spiral arms start to form. The spiral structure appears to be closely correlated with the flow pattern of the cloud
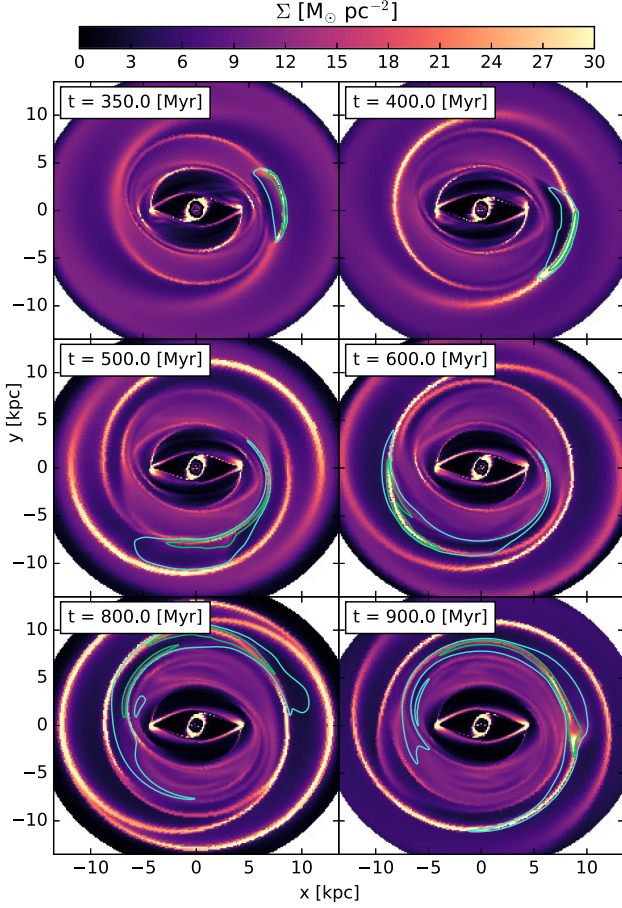
Figure 4. Snapshots of the surface density (Σ) for a fiducial inflow event which occured between $t = 305 - 325$ Myr with $M_c = 10^7$ M$_\odot$, $r_c = 1$ kpc, $r_{pos, 0} = 7.5$ kpc, $\phi_{pos, 0} = 0.0$ rad, and $f_c = -1.0$. Outer (blue) and inner (green) contours enclose 95 per cent and 50 per cent of the cloud mass, respectively.

Figure 5. Cloud's radial centre of mass (R_{com}) as a function of time for the fiducial simulation shown in Fig. 4. The shaded region roughly corresponds to the cloud's total radial extent.

Figure 6. $\langle A_1 \rangle$ for Fig. 4 from $t = 300$ Myr to $t = 2000$ Myr. The dashed red line corresponds to the cutoff value for lopsidedness suggested by Bournaud et al. (2005). The black line at the bottom of the figure shows $\langle A_1 \rangle$ from a simulation in which no inflow occurs.

material. At $t = 350$ Myr, we see that the cloud material moves away from corotation, and aligns itself with the newly forming spiral arm. By $t = 400$ Myr, the cloud is almost completely contained within the right spiral arm. Shortly thereafter, at $t = 500$ Myr, the majority of the cloud has shifted inwards on to the symmetric spiral arm. Past $t = 500$ Myr, the cloud is sheared substantially, and begins to take the shape of the inner spiral arm. Between $t = 800$ Myr and $t = 900$ Myr, much of the cloud material has again shifted between spiral arms. This oscillation of the cloud can be seen through an analysis of the cloud's centre of mass.

Fig. 5 shows the radial centre of mass (R_{com}) of the cloud as a function of time. The shaded region indicates $R_{com} \pm \sigma$, where σ is the standard deviation of the cloud mass distribution after integration over ϕ. We only allow radial bins that contain greater than 1 per cent of M_c, 10^5 M$_\odot$, to contribute to this measurement. The cloud migrates outward from $t = 300$ to $t = 400$ Myr. The cloud then reaches a maximum radius, and begins to oscillate between $R \approx 8.7$ kpc and $R \approx 8$ kpc for the next 400 Myr. Towards the end of the simulation, the cloud has been sheared in ϕ nearly over 2π. As a result, the oscillations of R_{com} are dampened. As the cloud shifts back and forth between radii, it moves through regions of high and low density. We should therefore see these oscillations in $\langle A_1 \rangle$.

Fig. 6 displays $\langle A_1 \rangle$ as a function of time. Clearly, $\langle A_1 \rangle$ shows oscillations, consistent with the radial motions of the cloud
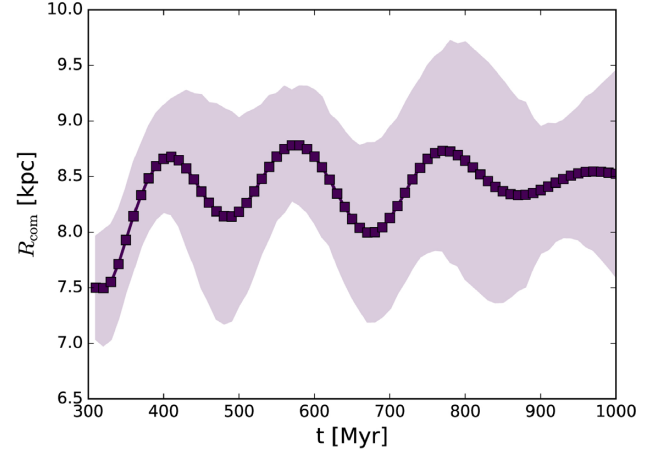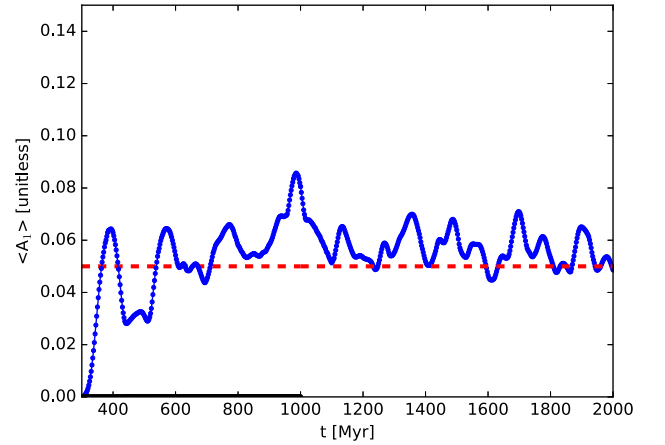
discussed above. While the magnitude of the lopsidedness is not particularly high ($\langle A_1 \rangle_{max} < 0.1$), $\langle A_1 \rangle$'s oscillatory structure provides a possible explanation for asymmetries seen in galaxies with no clear companion. The overall structure of this diagram is consistent with the evolution of surface density (Fig. 4). The initial peak around $t = 380$ Myr, comes from the initial infall. During this time, flow speed differences between disc gas and cloud material lead to an evacuation downstream of the cloud, but also create an overdense region near the forming spiral arm. When the cloud is eventually swept up by the gaseous disc, $\langle A_1 \rangle$ decreases, and the cloud is mostly contained in a symmetric spiral arm. At $t \approx 575$ Myr, the cloud material is driven inwards to a smaller radius and we see a second peak in $\langle A_1 \rangle$. At the end of the simulation $\langle A_1 \rangle$ appears to be increasing. We ran this particular simulation out to 2 Gyr, and while $\langle A_1 \rangle$ does not continually increase, it is oscillatory, with peaks of $\langle A_1 \rangle \approx 0.07$ and troughs around $\langle A_1 \rangle \approx 0.05$. The pattern described above seems to persist up to 2 Gyr.

This behaviour can be explained by the evolution of the manifolds discussed in the previous section. Upon cloud infall, a low density region is forming behind the cloud. This region is quickly heated to a temperature higher than the surrounding gas. This high pressure
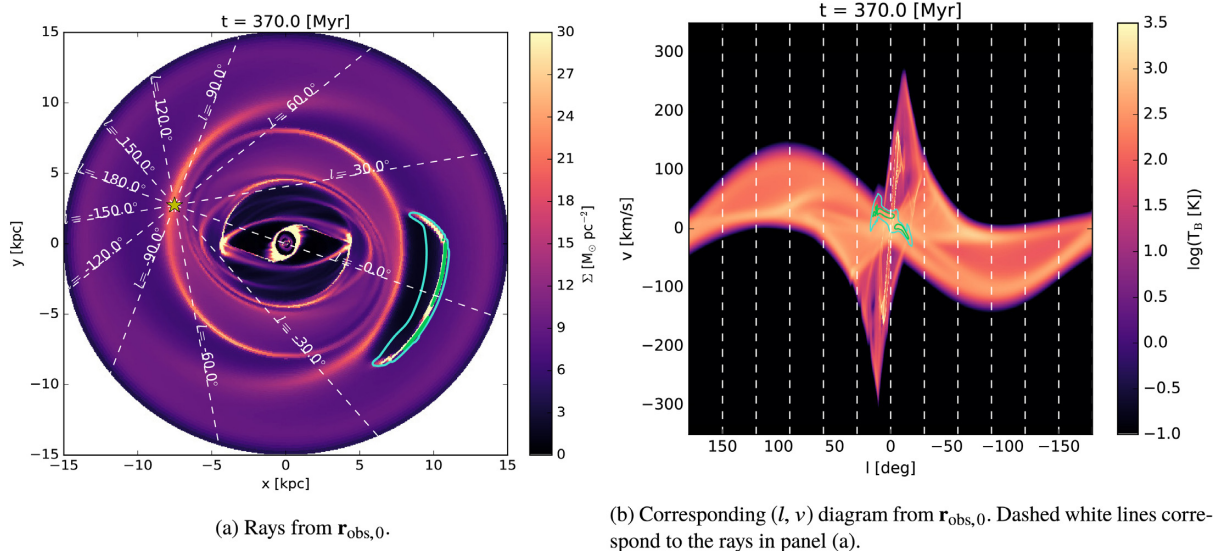
(a) Rays from $\mathbf{r}_{\mathrm{obs},0}$.

(b) Corresponding (l, v) diagram from $\mathbf{r}_{\mathrm{obs},0}$. Dashed white lines correspond to the rays in panel (a).

Figure 7. Ray structure and corresponding (l, v) diagram at $t = 370$ Myr for a simulation with all parameters the same as Fig. 4 except that $r_{\mathrm{pos},0} = 10$ kpc. Outer (blue) and inner (green) contours on density diagram enclose 95 per cent and 50 per cent of cloud mass, respectively. Outer (blue) and inner (green) contours on HI emission diagrams enclose 90 per cent and 50 per cent of total HI emission from the cloud material, respectively.

region pushes the gas that populates orbits on the manifold out to a larger radius ($t = 400$ Myr). This can be thought of as an initial driving force away from a stable minimum. The gas that has been knocked away from equilibrium seeks to return to equilibrium. However, during this time the manifolds have also been expanding outwards, to a point where the nearest equilibrium is now in the symmetric spiral arm. Therefore, the majority of the cloud material shifts downwards to a lower radius (to the symmetric spiral arm/manifold of orbits) ($t = 500$ Myr). In this manner, the initial infall of the cloud can be thought of as a driving force away from the manifold of orbits. What happens subsequently is a result of the gas trying to re-align itself with the manifolds, which are themselves evolving in time. This scenario appears to continue for the remainder of our simulation, though its effect at late times is dampened. For instance at $t = 800$ Myr, the cloud has again carved out a low density (and therefore high temperature) region that has pushed gas off of the manifold of orbits. The gas then 'corrects' this push by dropping to a lower radius, the aftermath of which is seen at $t = 900$ Myr.

To further analyse why the cloud migrates between arms throughout the simulation, we performed a simulation in which the cloud is not allowed to interact with the hydrodynamic variables at all, i.e. the cloud is a passive scalar field that evolves based on the values of density fluxes. This allows us to see how a parcel of gas will evolve in our static potential. The parcel of gas again seeks to align itself with the orbits of the manifold. However, because there is no low-density region carved out by the passive scalar field, the oscillations of the cloud are significantly reduced. The lag between the gas and the evolution of the manifolds is still present, but it is smaller because there is no initial 'driving force' behind the oscillation.

3.3 (l, v) diagram analysis

To determine whether infall signatures can be observed in edge-on gas discs, we calculate T_{B} as a function of observer angle, l, and line-of-sight velocity, v for a variety of observer positions.

3.3.1 An example (l, v) diagram

Fig. 7 provides a snapshot of the surface density and its corresponding (l, v) diagram from $\mathbf{r}_{\mathrm{obs},0}$, i.e an observer located at the position of the Sun. In this example, the parameters for the cloud inflow are the same as in Fig. 4, except that $r_{\mathrm{pos},0} = 10$ kpc. Overlaid on the density plot are the rays from the perspective of $\mathbf{r}_{\mathrm{obs},0}$. By matching Fig. 7(a) with Fig. 7(b), we can identify key features of the simulation in the (l, v) diagram. By far, the most prominent feature is the region of the bar, characterized by the parallelogram in (l, v) space. This region is confined to $l \sim \pm 30°$. The line-of-sight velocities peak at the tips of the semi-minor axis of the bar, and in this case they reach nearly ± 300 km s^{-1}. At low l, the inner ring of x_2 orbits is characterized by the bright, speckled, line that spans $v \sim \pm 180$ km s^{-1}. Our thermal model does not account for variations in the stellar radiation field, so this region is very dense and cold, contributing substantially to the emission. The 'speckled' structure, however, stems from the finite numerical resolution: velocity differences between cells in a coherent density structure are larger than the thermal broadening, thus the velocity field appears to have gaps (Heitsch 2013). While there are ways to address this problem (Shetty et al. 2011), it suffices here to point out the feature, because the region is of minor importance for our purposes. Moving away from the bar region, spiral arms become evident. In particular, for $-150° \lesssim l \lesssim -50°$, intensities are lower than at positive l, because the rays pass through lower density gas than the rays at positive l.

The cloud material provides another way for orientation. Contours on the density map enclose 95 per cent and 50 per cent of the cloud mass. Contours on the (l, v) diagram enclose 90 per cent and 50 per cent of the total cloud emission proportional to T_{B}. While the contours do not have an exact one-to-one correspondences, they help us locate the cloud in (l, v) space. Because all the cloud material is relatively constrained in radial velocity and because of its large distance from $\mathbf{r}_{\mathrm{obs},0}$, it appears in the (l, v) plot as a compact structure. From this perspective, the small flare at $l \approx 10°$ on the blue contour of Fig. 7(b) is the only evidence for the cloud infall.
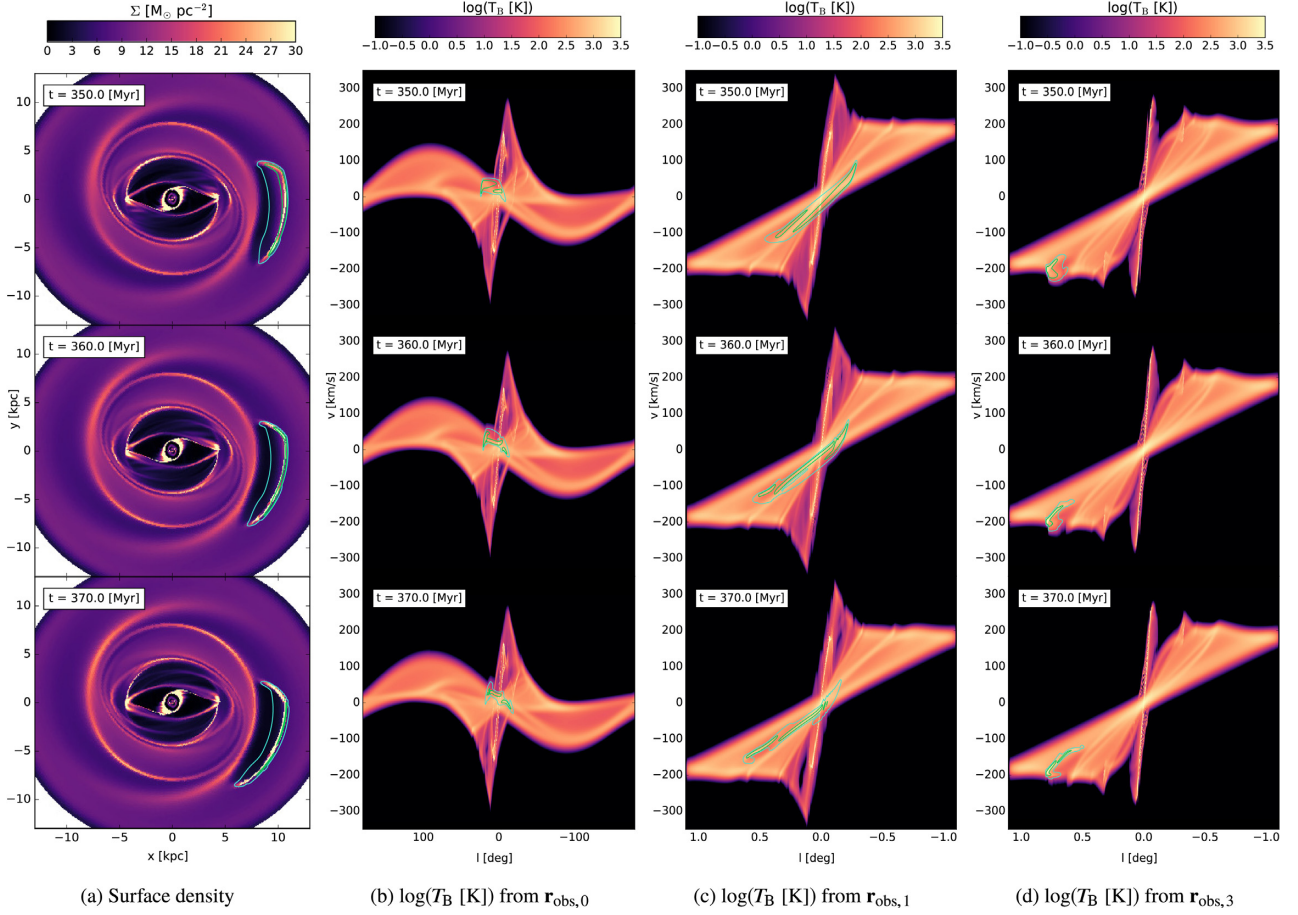
Figure 8. Surface density Σ and corresponding (l, v) diagrams with the same parameters as Fig. 7 at $t = 350, 360,$ and 370 [Myr] for three observer positions. Contours in these diagrams have the same definitions as those in Fig. 7.

Due to the large distance from the simulation domain, the rays for observer positions $\mathbf{r}_{obs, 1}$ and $\mathbf{r}_{obs, 3}$ are nearly parallel, covering an angle $\Delta l \approx 2°$. From $\mathbf{r}_{obs, 1}$ the rays are horizontal and enter from the right, such that $l > 0$ encompasses the bottom half of the simulation domain $(x, y < 0)$. When the cloud starts spreading out in the azimuthal direction, it also stretches in the line-of-sight velocity coordinate. For $\mathbf{r}_{obs, 3}$, the rays are vertical and enter from the top, such that $l > 0$ encompasses the right half of the simulation domain $(x > 0, y)$. Here, the line-of-sight velocity distribution of cloud material covers only a small range – the cloud is still coherently rotating.

3.3.2 Observing asymmetries in (l,v) diagrams

Fig. 8 shows three time instances, each for the observer positions $(\mathbf{r}_{obs, 0, 1, 3})$. We use these to assess whether the cloud would noticeably affect the (l, v) diagram, and thus, signatures of infall could be discovered. The three panels span a time range of only 20 Myr. The cloud is only marginally discernible from the disc material.

While we obviously can identify cloud material using the tracer fields, from $\mathbf{r}_{obs, 0}$, the impact of the cloud is only seen as a small 'flare' around $l \approx 10°$. Because the lines of sight connecting this observer with the cloud run through the centre of the Galaxy, T_B is largely dominated by the high gas densities in this region. This issue

is made even worse for $\mathbf{r}_{obs, 1}$. Here, the observer views the galaxy from the right. From this perspective, the cloud material is wholly contained in the gaseous envelope of the disc that is traced out by the tilted hour glass shape in the (l, v) plot. Any slight increase in T_B due to gas accretion is undetectable.

From the perspective of $\mathbf{r}_{obs, 3}$, however, there is a slight bump at positive l and negative v (top right panel of Fig. 8). This bump is due to the brief anomalous velocity the cloud introduces to the disc upon its entry. Yet, the perturbation is short-lived, and by $t = 370$ Myr, the cloud is already merging with the envelope of the disc. This suggests that cloud accretion on to discs may be observable as bumps in (l, v) diagrams. For instance, the bump at $t = 350$ Myr for $\mathbf{r}_{obs, 3}$ represents ~ 9 per cent increase in the total column density $N \propto \int T_B(v) dv$. As discussed, the perturbation is relatively short-lived, yet the apparent prevalence of HVCs in the Milky Way and other nearby galaxies suggests that HVC infall might be discernible in (l, v) diagrams.

To assess whether the cloud is detectable in a galaxy with ongoing star formation, we took the data from Fig. 8 and added 300 HI shells to it. We placed the shells randomly between 1 and 15 kpc, and assigned them a radius drawn from an exponential distribution with a scale of 175 pc (cf. fig 3 of Bagetakos et al. (2011)). Shells with radii greater than 300 pc were reduced by a factor of 1/2. We set the density of a HI shell by distributing the column density inside the shell evenly over the rim of the shell, mimicking swept-up material. The shell temperature is set to the equilibrium temperature at the
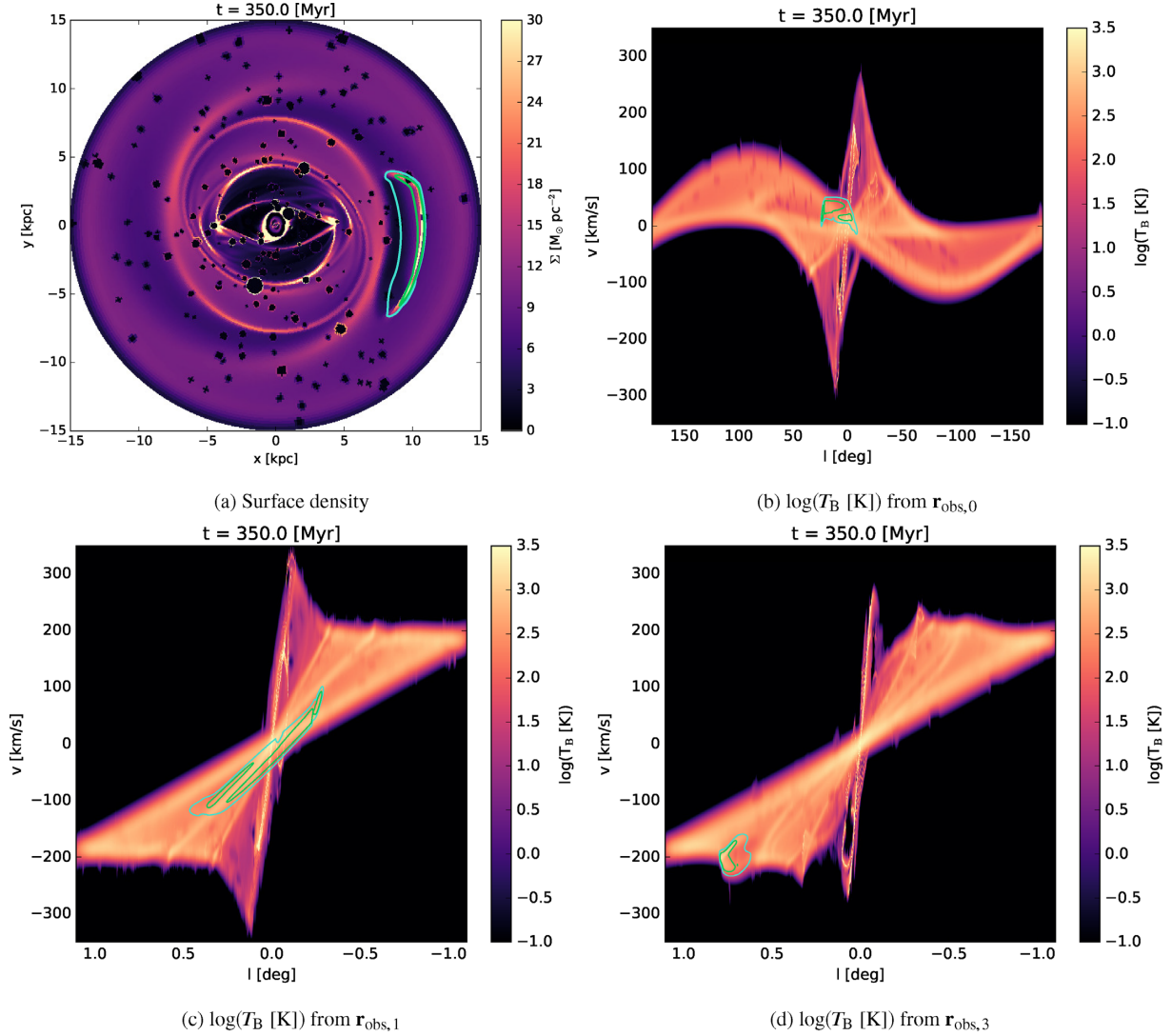
(a) Surface density

(b) $\log(T_B \text{ [K]})$ from $\mathbf{r}_{\text{obs},0}$

(c) $\log(T_B \text{ [K]})$ from $\mathbf{r}_{\text{obs},1}$

(d) $\log(T_B \text{ [K]})$ from $\mathbf{r}_{\text{obs},3}$

Figure 9. (l, v) diagrams for a noisy disc corresponding to the simulation presented in the top panel of Fig. 8. Here, we have placed 300 HI shells in the disc and recomputed the (l, v) diagrams from each observer.

corresponding density. We assume shell expansion at a randomly selected velocity of $10 < v < 30$ km s^{-1}. Fig. 9 shows the recomputed (l, v) diagrams for this noise disc. Holes in the HI distribution appear as small 'blips' of decreased intensity in the (l, v) diagram. Large shells, particularly those that have swept up a large amount of mass, radiate strongly in HI due to their high density and low temperature. Though the shells introduce noise in the (l, v) diagram, the effects of the cloud can still be discerned in Fig. 9(d) as a bump of anomalous velocity ($l \approx 0.75$) discussed in the previous paragraph.

3.3.3 (l, v) diagrams for fiducial simulation

The three right panels of Fig. 10 show the (l, v) diagrams for the fiducial simulation. Depending on observer position, the HVC initially introduces an asymmetry in T_B. For instance, from the perspective of $\mathbf{r}_{\text{obs}, 3}$ at $t = 350$ Myr, the high density region that forms as the cloud pushes gas out to larger radii increases T_B by a factor of $\sim$3 at $l = 0.5$ and $v \approx -200$ km s^{-1} when compared to T_B at $l = -0.5$ and $v \approx 200$ km s^{-1}. Yet, this increase in T_B is transient,

as the cloud is quickly sheared such that it appears at both negative and positive l, negating any chance of detecting an asymmetry.

3.4 Parameter influence

For face-on galaxies, we use $\langle A_1 \rangle$ to assess the influence of model parameters on disc asymmetries. Fig. 11 shows $\langle A_1 \rangle$ for three simulations accreting the HVC at $r_{\text{pos}, 0} = 7.5$ kpc, but at different azimuthal cloud velocities parameterized by f_c. For positive f_c the cloud is orbiting against the bar rotation. Because $r_{\text{pos}, 0}$ is outside of corotation, the cloud orbits with the gas flow. For $f_c = 1$ the cloud has a zero velocity in the inertial frame, while for $f_c = 2$, the cloud has a velocity of $\sim$250 km s^{-1} in the inertial frame, approximately matching that of the gas.

Because the cloud accretes on to the disc in the same spot for each of these simulations, the shape of $\langle A_1 \rangle$ for all values of f_c is very similar for the first 300 Myr. In the case of $f_c = 1$, the amplitude is decreased substantially. The velocity is much lower in this case, so the cloud does not initially sweep out a large angle in ϕ. Instead the cloud is fairly contained. As $\langle A_1 \rangle$ is computed
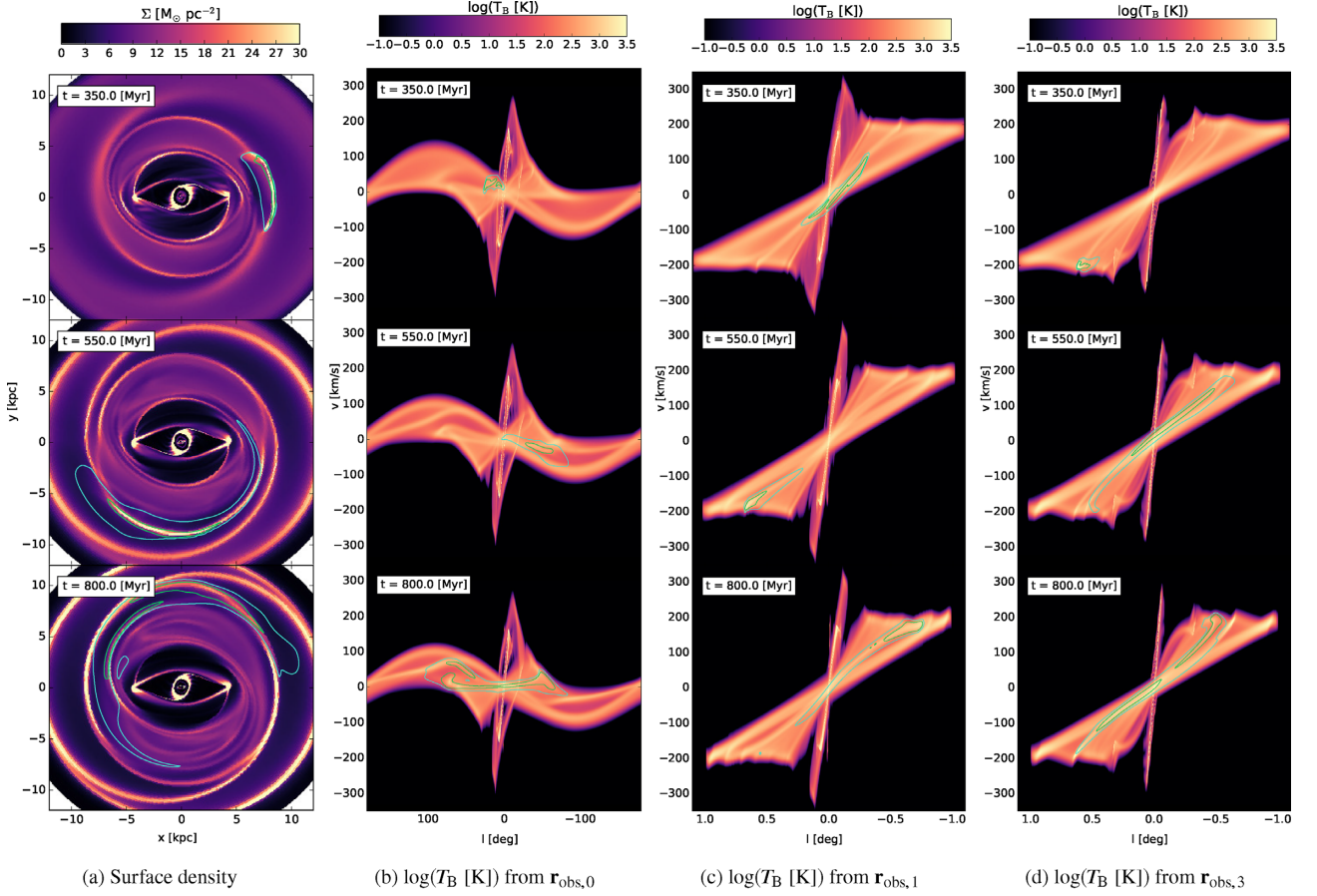
(a) Surface density

(b) $\log(T_B \, [\mathrm{K}])$ from $\mathbf{r}_{\mathrm{obs},0}$

(c) $\log(T_B \, [\mathrm{K}])$ from $\mathbf{r}_{\mathrm{obs},1}$

(d) $\log(T_B \, [\mathrm{K}])$ from $\mathbf{r}_{\mathrm{obs},3}$

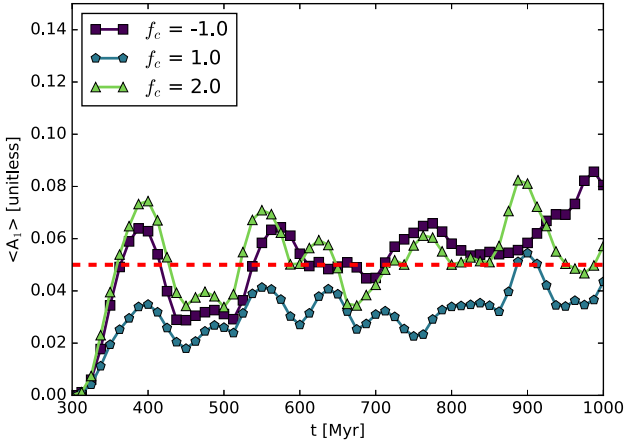**Figure 10.** (l, v) diagrams for the fiducial simulation shown (see Fig. 4).

Figure 11. $\langle A_1 \rangle$ against time for three values of the cloud orbit parameter f_c. All other parameters are kept the same and are identical to the model shown in Fig. 4. The dotted red line indicates the cutoff value for lopsidedness suggested by Bournaud et al. (2005).

Figure 12. $\langle A_1 \rangle$ against time for four values of the cloud radius. All other parameters are kept the same and are identical to the model shown in Fig. 4. The dotted red line indicates the cutoff value for lopsidedness suggested by Bournaud et al. (2005).

from an integral over ϕ and then averaged over R, the overall amplitude of $\langle A_1 \rangle$ decreases. For $f_c = 2$, the velocity (in the inertial frame) is of the same amplitude as that of $f_c = -1$, therefore their $\langle A_1 \rangle$ values are similar. Further, the three $\langle A_1 \rangle(t)$ evolve similarly, supporting our interpretation of the cloud migrating between orbits (see Section 3.2).
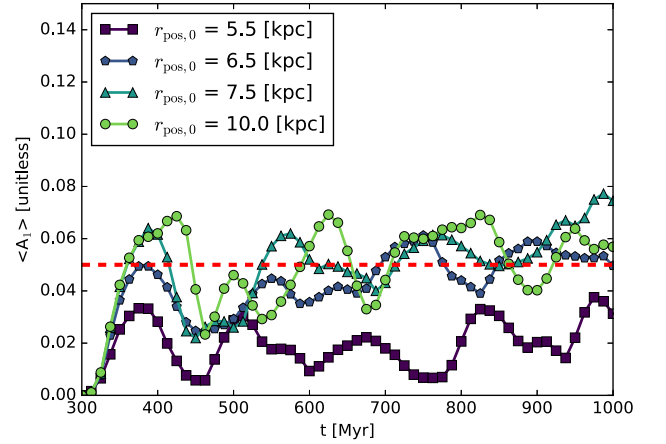
Fig. 12 shows the effect of the initial positions for the cloud at fixed $f_c = -1$ and $r_c = 1$ kpc. The curves behave largely the same, oscillating with time. The cloud's initial position can have an influence on the amplitude of $\langle A_1 \rangle$. In particular, max $(\langle A_1 \rangle)$ seems to increase with increasing cloud position. For $r_{\mathrm{pos},0} = 5.5$ kpc, because the cloud is confined to low radii, and the region of the disc is symmetric, the cloud does not give rise to large-scale
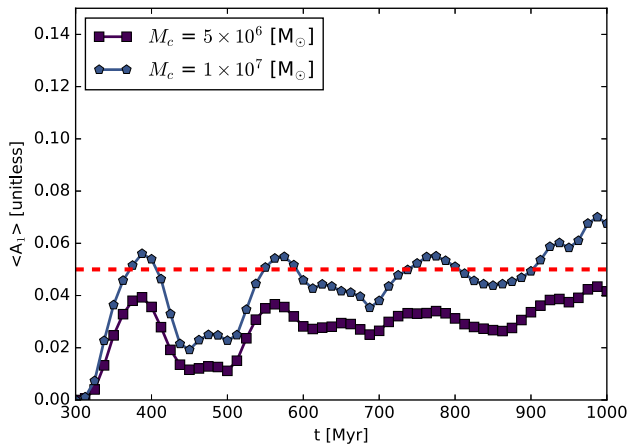
Figure 13. $\langle A_1 \rangle$ against time for two values of the cloud mass. All other parameters are kept the same and are identical to the model shown in Fig. 4, except here $r_c = 500$ pc. The dotted red line indicates the cutoff value for lopsidedness suggested by Bournaud et al. (2005).

asymmetries. The same argument can be made for $r_{pos, 0} = 6.5$ kpc, though we see that as time increases, the cloud spans a greater region in R, increasing $\langle A_1 \rangle$. Fig. 13 shows the effect of the mass of the cloud on $\langle A_1 \rangle$. As expected, a lower mass yields a lower amplitude in $\langle A_1 \rangle$. The structure of the oscillations in $\langle A_1 \rangle$ remains the same.

4 DISCUSSION AND CONCLUSIONS

We present a set of hydrodynamical simulations exploring the effect of mass inflow on the gas distribution in barred spiral galaxies. We assess the impact of mass inflow via (l, v) diagrams and by determining the lopsidedness parameter, A_1 (Rix & Zaritsky 1995; Bournaud et al. 2005; Jog & Combes 2009). While the effect of mass infall is clearly visible in the surface density maps (e.g. left column of Fig. 4), a cloud of 10^7 M$_\odot$ can only be detected in the (l, v) diagrams immediately after infall. Yet, infall can lead to detectable lopsidedness, especially in terms of $\langle A_1 \rangle$. Bournaud et al. (2005) explored lopsidedness in the stellar component caused by tidal encounters, galactic collisions, and cosmic gas accretion. Here, we focus on whether accretion of a HVC on to the disc can contribute to lopsidedness in a galaxy's gas distribution. In particular, we have examined how a non-axisymmetric potential affects gas disc lopsidedness in the outer regions of a barred-spiral galaxy.

We find that infall events can affect the symmetry of a galactic disc for ∼1.5 Gyr. While the cloud is sheared in the differentially rotating gas disc, its centre of mass shifts back and forth between spiral arm patterns, resulting in an oscillatory lopsidedness. A peak in lopsidedness typically lasts for ∼50 Myr (Fig. 6). While the amplitude of the lopsidedness parameter $\langle A_1 \rangle$ depends strongly on the parameters of the cloud infall, the oscillatory structure of $\langle A_1 \rangle$ occurs in all of our models. These oscillations appear to arise from a lag between the manifold of orbits (see Romero-Gomez et al. 2006) and the gas.

Inflow events do disrupt the x_1 family of orbits substantially. In some cases, the additional material can enhance the density at the bar ends. This is particularly true for those of our models with $r_{pos, 0} = 5.5$ kpc, as the material is able to reach the bar ends. Exploring the consequences on star formation activity in these regions is beyond the scope of this work.

Our models suggest that the position of the infall ($r_{pos, 0}$), the azimuthal velocity component of the cloud (parametrized by f_c), and the cloud mass (M_c) have the strongest influence on lopsidedness. As can be seen from Figs 11 and 12, the initial cloud radius has little dynamical influence, unless $r_c > 1$ kpc (Figs 11 and 12). Tests with $r_c > 1$ kpc yielded low amplitudes in $\langle A_1 \rangle$. The cloud mass strongly affects the amplitude of $\langle A_1 \rangle$ (Fig. 13). For a lower mass of $M_c = 5 \times 10^6$ M$_\odot$, the amplitude of the lopsidedness is reduced, peaking at only $\langle A_1 \rangle = 0.04$, and thus rendering its detection unlikely.

Finally, HVC accretion events can result in long lived (∼1.5 Gyr), low amplitude disc lopsidedness. This is a non-negligible result, but due to the low amplitudes it is not enough to explain the largepercentages of lopsided galaxies seen at a variety of redshifts (Bournaud et al. 2005; Reichard et al. 2008; Jog & Combes 2009). Our results suggest that gas infall can contribute to observed lopsidedness in gaseous distributions. Yet, it is also clear that infall is unlikely to be a dominant source of lopsidedness. Evidence of recent cloud accretion may be visible as bumps in the terminal velocity curves of edge-on galaxies.

We calculate lopsidedness from the simulated gas emission, rather than from the stellar light distribution. Because the stellar mass component is implemented as a static gravitational potential, it cannot contribute to lopsidedness in our models. This limitation could be remedied with a live stellar and dark matter component. Given that the HVC mass is small compared to the overall disc mass, this seems unlikely. However, the situation may change if the infalling HVC had its own dark matter halo, as suggested by e.g. Braun & Burton (1999); Blitz et al. (1999); Nichols et al. (2014).

REFERENCES

Athanassoula E., 1992a, MNRAS, 259, 328
Athanassoula E., 1992b, MNRAS, 259, 345
Bagetakos I., Brinks E., Walter F., de Blok W. J. G., Usero A., Leroy A. K., Rich J. W., Kennicutt R. C., 2011, AJ, 141, 23
Baldwin J. E., Lynden-Bell D., Sancisi R., 1980, MNRAS, 193, 313
Bensby T., Feltzing S., Lundström I., 2003, A& A, 410, 527
Binney J., Merrifield M., 1998, Galactic Astronomy. Princeton University Press, p. 9
Binney J., Tremaine S., 2011, Galactic Dynamics. Princeton University Press, p. 20
Binney J., Gerhard O. E., Stark A. a., Bally J., Uchida K. I., 1991, MNRAS, 252, 210
Blitz L., Spergel D. N., Teuben P. J., Hartmann D., Burton W. B., 1999, ApJ, 514, 818
Bournaud F., Jog C. J., Combes F., 2005, A& A, 437, 69
Braun R., Burton W. B., 1999, A& A, 341, 437
Bryan G. L. et al., 2014, ApJS, 211, 19
Contopoulos G., Papayannopoulos T., 1980, A&A, 92, 33
Dopita M. A., Sutherland R. S., Nicholls D. C., Kewley L. J., Vogt F. P. A., 2013, ApJS, 208, 10
Dopita M. A., Kewley L. J., Sutherland R. S., Nicholls D. C., 2016, Astrophys. Space Sci., 361, 61

Eskridge P. B. et al., 2000, AJ, 119, 536

Fox A. J. et al., 2016, ApJ, 816, L11

Goodson M. D., Luebbers I., Heitsch F., Frazer C. C., 2016, MNRAS, 462, 2777

Gottlieb S., Shu C.-w., 1998, Math. Comput., 67, 73

Heitsch F., 2013, ApJ, 769, 115

Jog C. J., Combes F., 2009, Phys. Rep, 471, 75

Jung M., Illenseer T. F., Duschl W. J., 2018, Astron. Astrophys.

Kim C.-G., Ostriker E. C., Kim W.-T., 2014, ApJ, 786, 64

Kim S. S., Saitoh T. R., Jeon M., Figer D. F., Merritt D., Wada K., 2011, ApJ, 735, 5

, Kim W. T., Seo W. Y., Stone J. M., Yoon D., Teuben P. J., 2012, ApJ, 747, 60

Koyama H., Inutsuka S.-i., 2002, ApJ, 564, L97

Lockman F. J., Benjamin R. A., Heroux A. J., Langston G. I., 2008, ApJ, 679, L21

Nichols M., Bland-Hawthorn J., 2009, ApJ, 707, 1642

Nichols M., Mirabal N., Agertz O., Lockman F. J., Bland-Hawthorn J., 2014, MNRAS, 442, 2883

Pedicelli S. et al., 2009, A& A, 504, 81

Pfenniger D., 1984, A&A, 134, 373

Putman M., Peek J., Joung M., 2012, Annu. Rev. A&A, 50, 491

Reichard T. A., Heckman T. M., Rudnick G., Brinchmann J., Kauffmann G., 2008, ApJ, 677, 186

Ridley M. G. L., Sormani M. C., Treß R. G., Magorrian J., Klessen R. S., 2017, MNRAS, 469, 2251

Rix H.-W., Zaritsky D., 1995, ApJ, 447, 82

Romero-Gomez M., Masdemont J. J., Athanassoula E., Garcia-Gomez C., 2006, A& A, 453, 8

Romero-Gómez M., Athanassoula E., Masdemont J. J., García-Gómez C., 2007, A& A, 472, 63

Sancisi R., Fraternali F., Oosterloo T., van der Hulst T., 2008, A&A Rev., 15, 189

Shetty R., Glover S. C., Dullemond C. P., Ostriker E. C., Harris A. I., Klessen R. S., 2011, MNRAS, 415, 3253

Skinner M. A., Ostriker E. C., 2010, ApJS, 188, 290

Sormani M. C., Binney J., Magorrian J., 2015, MNRAS, 449, 2421

Sormani M. C., Treß R. G., Ridley M., Glover S. C. O., Klessen R. S., Binney J., Magorrian J., Smith R., 2018, MNRAS, 475, 2383

Stone J. M., Gardiner T. a., Teuben P., Hawley J. F., Simon J. B., 2008, ApJS, 178, 137

Sutherland R. S., Dopita M. A., 1993, ApJS, 88, 253

Thilker D. A., Braun R., Walterbos R. A. M., Corbelli E., Lockman F. J., Murphy E., Maddalena R., 2004, ApJ, 601, L39

Toro E. F., Spruce M., Speares W., 1994, Shock Waves, 4, 25

Wada K., Koda J., 2004, MNRAS, 349, 270

Wakker B. P. et al., 2008, ApJ, 672, 298

Wakker B. P. et al., 2007, ApJ, 670, L113

Wakker B. P., van Woerden H., 1997, ARA&A, 35, 217

Zaritsky D., Rix H., 1997, ApJ, 477, 118

This paper has been typeset from a TEX/LATEX file prepared by the author.